Self-balanced Two-output Battery Charger

Christian Branas
Electronics Technology, Systems and Automation Engineering Department (TEISA)
Universidad de Cantabria
Santander, Spain
branasc@unican.es

Francisco J. Azcondo
Electronics Technology, Systems and Automation Engineering Department (TEISA)
Universidad de Cantabria
Santander, Spain
azcondof@unican.es

Alberto Pigazo
Deparment of Computer Science and Electronics
Universidad de Cantabria
Santander, Spain
pigazoa@unican.es

Rosario Casanueva
Electronics Technology, Systems and Automation Engineering Department (TEISA)
Universidad de Cantabria
Santander, Spain
casanuer@unican.es

Francisco J. Díaz
Electronics Technology, Systems and Automation Engineering Department (TEISA)
Universidad de Cantabria
Santander, Spain
javier.diaz@unican.es

Paula Lamo
Escuela Superior de Ingeniería y Tecnología
Universidad Internacional de la Rioja
Logroño, Spain
paula.lamo@unir.net

***Abstract*— The design and modeling of a self-balanced two-output battery charger capable to charge two high-power LiFePO4 battery packs is presented. The proposal is based on a four-phase resonant converter, which is designed as a voltage-controlled current-source, working at constant switching frequency. The output stage consists of a transformer with a single primary and two secondaries implementing two current-doubler rectifiers. The structure of the output stage naturally imposes the self-balance-of-charge of both battery packs provided that the coupling between the primary and each of the secondaries has a negligible mismatch. The electrical model of the battery is used to study the batteries charge equalization during the charging process considering the non-idealities of the output transformer. The theoretical analysis and design procedure of the proposed battery charger is fully explained. The output current capability and efficiency are validated experimentally considering a 50 Ah 48 V commercial battery pack.**

Keywords—Power electronics, battery chargers, resonant power conversion, batteries, HF transformers

I. INTRODUCTION

Multi-output battery chargers are a cost-effective choice to speed-up the charging process in facilities where storage systems are widely used such as data centers and renewable energy systems [1]. Specifications that become design challenges for chargers of high-current capacity are to achieve the highest efficiency and reliability of the power conversion circuit. In this paper, the proposed solution is based on a multi-phase resonant converter, shown in Fig.1. The multi-phase approach of the inverter stage reduces the conduction loss and enables the control of the charging current at constant switching frequency by shifting the phase of the output voltages $V_{1,2,3,4}$ of each class *D* section of the inverter [2].

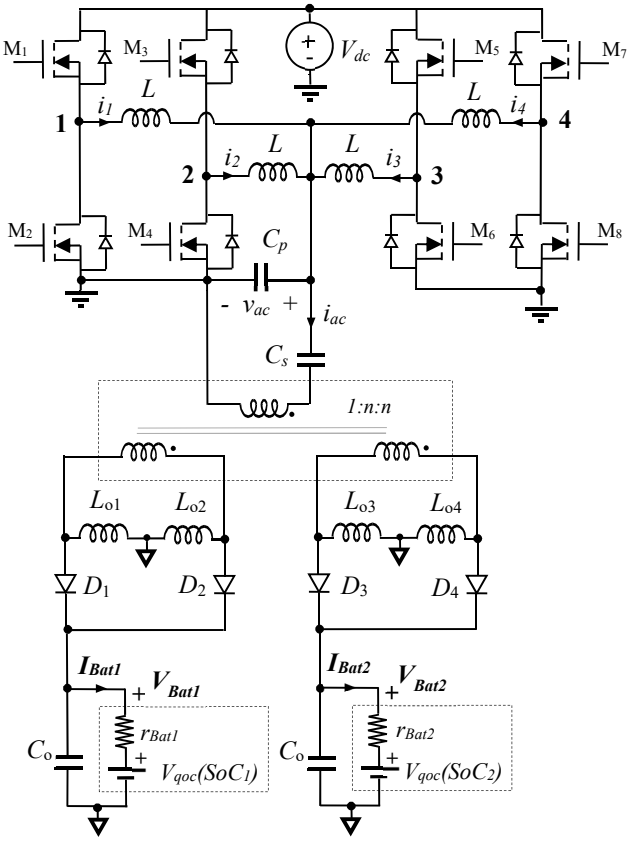

Fig. 1. Two-output battery charger

This work was supported by the Spanish Ministry of Science and Innovation and the European Commission under the research project PID2021-128941OB-I00 "Efficient Energy Transformation in Industrial Environments".

The output stage consists of a multi-winding transformer with secondaries feeding two current-doubler rectifiers providing the charging current to each battery. The batteries are represented in steady-state by their internal DC resistance, r_{Bat}, in series with their quasi open-circuit voltage at a given State-of-Charge (*SoC*), $V_{qoc}(SoC)$. The balance-of-charge of both battery packs is naturally achieved, if coupling between primary and both secondaries are essentially the same, due to the power balance principle among the transformer's windings. For this application, the transformer-based equalization [3-4] is well suited considering that only two battery packs are connected at the same time. The built-in battery management system (BMS) guarantees the electrical safety and protection at the cell level [4].

The charger is designed to meet the specifications recommended for a $LiFePO_4$ commercial battery pack with 48 V nominal voltage and 50 Ah nominal capacity (C_n), i.e. the 48NPFC50. The charging protocol for $LiFePO_4$ batteries is the constant current (CC) - constant voltage (CV) [5]. Three experimental charging profiles, shown in Fig. 2, were obtained in a battery laboratory facility. The maximum battery voltage during charging is limited at $V_{B(max)}$ =53.5 V.

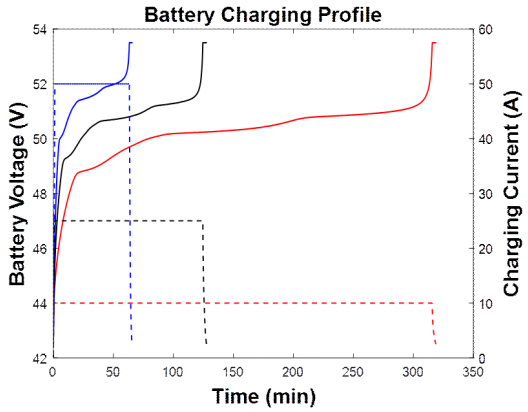

Fig. 2. Experimental charging profiles at 10 A (red), 25 A (black) and 50 A (blue) for a 48NPFC50 $LiFePO_4$ battery.

The user manual recommends a conservative value, $C_n/5$, as the charging current rate, however, $LiFePO_4$ technology tolerates fast-charging protocols [5]. In this work, a total output current capability, I_B = 20 A, is considered for designing the charger.

II. Four-phase Two-outputs LC_pC_s Resonant Converter

The circuit analysis is carried out assuming the first harmonic approximation (FHA) [2]. Considering the converter symmetry, the circuit is simplified as it is shown in Fig. 3, where R_{ac} is the input impedance of the DC output stage reflected into de AC side.

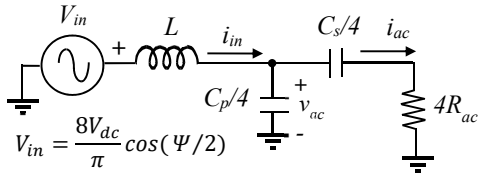

Fig. 3. Simplified circuit of the resonant inverter stage.

Among several modulation schemes, the control of the converter is carried out adjusting the phase shift of the midpoint voltages $V_{1,2,3,4}$ by pairs. In this way, the control angle, Ψ, is defined as the phase shift from $V_{1,2}$ to $V_{3,4}$. From the phasor analysis, the resonant inverter stage of the converter is fully characterized by the parameters summarized in Table I.

TABLE I. Parallel Parameters of the LC_pC_s Resonant Converter

Resonant frequency	Characteristic impedance	Quality factor
$\omega_p = \frac{1}{\sqrt{\frac{LC_p}{4}}}$	$Z_p = \omega_p L = \frac{4}{\omega_p C_p}$	$Q_p = \frac{4R_{ac}}{Z_p}$

The resonant converter is designed as a voltage-dependent current source. Using this approach, the circuit presents an inherent maximum current limitation which is a safer operation mode for battery chargers. The LC_pC_s resonant inverter achieves a current source behavior working at the parallel resonant frequency, ω_p, while preserving the zero-voltage switching mode (ZVS) for a wide load range [2]. The amplitude of the phasor of the primary side current, $\hat{I}_{ac}$, as a function of the DC-link voltage, V_{dc}, parallel resonant tank impedance, Z_p, and the control parameter, Ψ, is obtained in (1)

$$\hat{I}_{ac} = \frac{8V_{dc}}{\pi Z_p} cos(\Psi/2) \tag{1}$$

A. Design of the Resonant Inverter Stage.

The switching losses are minimized by ensuring the ZVS mode of the transistors on the primary side of the converter [2]. The ZVS mode requires sufficient phase-delay of the resonant current, i_{in}, with respect to the input voltage, v_{in}. The minimum value of power factor angle for achieving ZVS, φ_{zvs}, is given in (2) and depends on the dead time, t_d, of the transistors' driver and ω_p [2].

$$\varphi_{zvs} = \frac{t_d \omega_p}{2\pi} \cdot 360^0 \tag{2}$$

As design criterium, a value of power factor angle $\phi_i = 2\varphi_{zvs}$ is assumed at nominal conditions for achieving a reliable operation of the converter. The transformer's turn ratio, n, to meet such condition is calculated according to (3).

$$n = \frac{\pi^2 V_{Bat(Max)} \, tan\, 2\, \varphi_{zvs}}{2V_{dc}} \tag{3}$$

The multiphase solution for the resonant inverter stage achieves an efficiency higher than 90% even at relatively low values of V_{dc} and using low-cost transistors. The maximum efficiency of the resonant inverter stage is obtained at $\Psi = 0^o$ at the boundary between CC and CV stages, where the total output power P_B is the maximum, P_B = 1.07 kW.

$$\eta_I = \frac{1}{1 + \frac{\pi^2 r P_B}{8V_{dc}^2}(1 + tan\, 2\, \varphi_{zvs})} \tag{4}$$

The efficiency given in (4) is obtained considering the conduction loss only, which is represented by the resistance r = 1.5 Ω.

The converter is supplied from DC-link voltage, V_{dc} = 400 V. The switching frequency is $\omega_p = 2\pi(125\text{ kHz})$. The dead time of the driving signals is t_d = 650 ns for a $\varphi_{zvs} = 29^o$. The maximum charging battery voltage is $V_{Bat(max)}$ = 53.5 V. Upon substitution in (3), the transformer's turns ratio is $n = 1$. The maximum current for each output is $I_{Bat1,2(max)}$ = 10 A at $\Psi = 0^o$, being the total current $I_B = I_{Bat1}+I_{Bat2}$ = 20 A. Considering that $\hat{I}_{ac}=2nI_B/\pi$ = 12.7 A and substituting in (1), the parallel characteristic impedance is, Z_p = 80 Ω. Finally, from Table I: L = 100 µH and C_p = 64 nF. Using (4), the efficiency of the resonant inverter stage is η_I = 0.968.

B. Design of the Output Stage

The current-doubler rectifier is chosen searching the best performance for high current applications by reducing the transformer current. The low output voltage of this application enables the use of Schottky diodes, avoiding any control circuit in the secondary side. The current-doubler rectifier is shown in Fig. 4. For design purposes, an ideal transformer and a lossless circuit are considered.

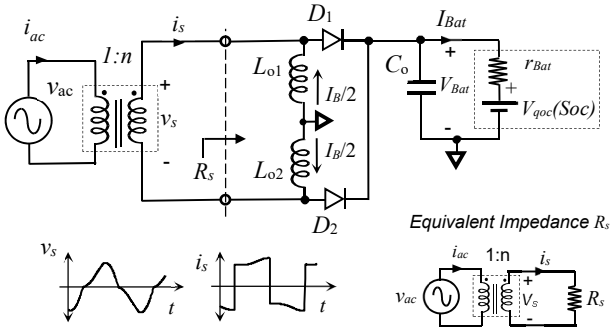

Fig. 4. Current-doubler rectifier and theoretical waveforms considering an ideal transformer.

The conduction time, t_1, of diodes D_1 and D_2 is obtained from the volts-seconds balance across the filter inductors L_{o1} and L_{o2}. The areas are calculated according to the approximation shown in Fig. 5.

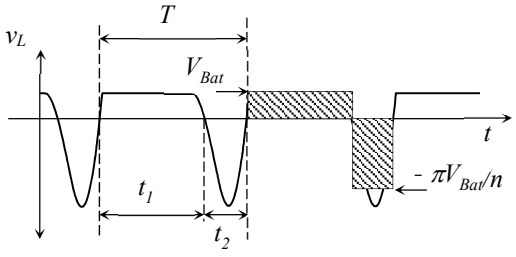

Fig. 5. Theoretical voltage waveform in the inductors filter L_{o1} and L_{o2}.

$$t_1 = \frac{\pi}{n+\pi}T \tag{5}$$

The amplitude of the current ripple in each inductor is determined by,

$$\Delta i_L = \frac{\pi^2 V_{Bat(Max)}}{(n+\pi)\omega_p L_o} \tag{6}$$

From (7), the ripple of the charging current is a function of the switching frequency, the output filter components and battery parameters.

$$\Delta i_{Bat} = \frac{\pi^3 V_{Bat(Max)}}{16(n+\pi)r_{Bat}\omega_p^2 L_o C_o} \tag{7}$$

The limitation of the output current ripple, Δi_{Bat}, is imposed to avoid the battery degradation. The filter inductors are Vishay IHLP-8787MZ with L_o = 75 µH and r_{LF} = 30 mΩ at 25º C. From (6), the amplitude of the current ripple in each inductor is Δi_L = 2.16 A. The r_{Bat} is estimated at 40 mΩ. The output capacitor, C_o, is calculated to achieve a maximum current ripple equal to 0.1% of the charging current, Δi_{Bat} = 10 mA. From (7), C_o = 390 µF.

Since the output filter removes the high-frequency ripple, Δi_{Bat}, the low ripple approximation is used to study the rectifier in steady-state. Using the first harmonic of the secondary side current, i_s, the amplitude of the current as a function of the DC output current is given in (8).

$$\hat{I}_s = \frac{2I_{Bat}}{\pi} \tag{8}$$

The amplitude of the voltage at the secondary side of the transformer is obtained as a function of the battery parameters,

$$\hat{V}_s = \pi V_{Bat} = \frac{\pi^2}{2} r_{Bat}\hat{I}_s + \pi V_{qoc} \tag{9}$$

From (8) and (9), the current-doubler rectifier represents an equivalent load, R_s, connected at the secondary side of the transformer,

$$R_s = \frac{\pi^2}{2}R_{Bat} = \frac{\pi^2}{2}\left(r_{Bat} + \frac{V_{qoc}}{I_{Bat}}\right) \tag{10}$$

The equivalent resistance reflected in the primary side, R_{ac} considering both current doubler rectifiers is obtained as,

$$R_{ac} = \frac{\pi^2}{2n^2}\left(\frac{R_{s1}R_{s2}}{R_{s1}+R_{s2}}\right) \tag{11}$$

C. Transformer modeling

The asymmetries at the output stage leads to unequal *SoC* for each battery packs when the charging process ends. Tolerances of the inductor filters and capacitors show little effect on the charge equalization, as the extraction of the mean value of all variables is performed correctly.

However, the final *SoC* of each battery packs strongly depends on any mismatch between the secondaries of the transformer, which is the main drawback of the transformer-based cell equalization [4]. In this case, the low transformer turns ratio, n = 1, makes achievable the implementation with very low parameter dispersion. The transformer has been built with an ETD49 core of material N87. All windings consist of 16 turns of 42 twisted AWG 32 strands. The primary, W_1; is placed in the middle, between the secondaries, W_2 and W_3. The three-windings transformer is modeled using the extended cantilever model [6] which it is shown in Fig. 6.

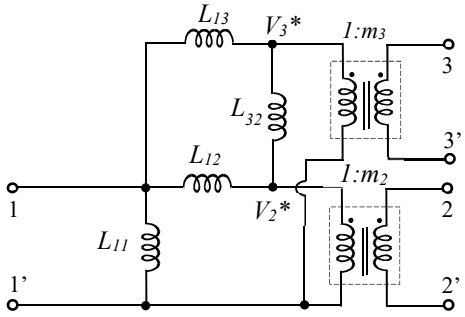

Fig. 6. Full order extended cantilever model of the three-winding transformer.

All parameters of the full order extended cantilever model can be measured directly following the procedure explained in [6]. However, it can be considered that using the transformer within a battery charger and even under an extreme charge unbalance, the voltage of the batteries is similar, allowing the model order to be reduced. Moreover, as the charging process progresses, the voltage difference tends to disappear. In this way, the reflected voltages V_2* and V_3* are approximately equal and the inductance L_{32} can be removed from the model. The reduced order model is shown in Fig. 7.

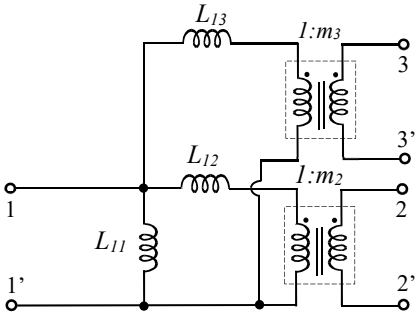

Fig. 7. Reduced order model of the three-winding transformer.

To extract the parameters of the reduced order model, the open-circuit and short-circuit tests [6] are applied in windings 1-1', 2-2' and 3-3'. Six inductances, summarized in Table II, are obtained where, L_{xo} is the inductance seen from winding x-x' with the others open and L_{xk} is the inductance measured from winding x-x' with the others short-circuited.

TABLE II. OPEN-CIRCUIT AND SHORT-CIRCUIT TESTS INDUCTANCES

L_{xo}	L_{xk}
$L_{1o} = L_{11}$	$L_{1k} = L_{11}\|\|L_{12}\|\|L_{13}$
$L_{2o} = (m_2)^2(L_{11} + L_{12})$	$L_{2k} = (m_2)^2 L_{12}$
$L_{3o} = (m_3)^2(L_{11} + L_{13})$	$L_{3k} = (m_3)^2 L_{13}$

The measurement is carried out at 100 kHz to make the R_{dc} of the windings negligible. The result of applying the open-circuit and short-circuit tests is summarized in Table III.

TABLE III. RESULT OF THE OPEN-CIRCUIT AND SHORT-CIRCUIT TESTS

L_{1o}	L_{1k}	L_{2o}	L_{2k}	L_{3o}	L_{3k}
770µH	0.74 µH	771µH	1.55 µH	868µH	1.55 µH

Working with Table II, the inductances of the reduced order model L_{11}, L_{12} and L_{13} as well as the effective transformer ratios m_2 and m_3 are obtained as a function of the measured inductances, L_{1o}, L_{1k}, L_{2o}, L_{2k}, L_{3o}, and L_{3k}.

$$L_{11} = L_{1o} \tag{12}$$

$$L_{12} = \frac{L_{1o}L_{2k}}{L_{2o} - L_{2k}} \tag{13}$$

$$L_{13} = \frac{L_{1o}L_{3k}}{L_{3o} - L_{3k}} \tag{14}$$

$$m_2 = \sqrt{\frac{L_{2o}}{L_{1o}}\left(1 - \frac{L_{2k}}{L_{2o}}\right)} \tag{15}$$

$$m_3 = \sqrt{\frac{L_{3o}}{L_{1o}}\left(1 - \frac{L_{3k}}{L_{3o}}\right)} \tag{16}$$

The parameters of the reduced-order cantilever model of the three-windings transformer are given in Table IV.

TABLE IV. PARAMETERS OF THE CANTILEVER MODEL

L_{11}	L_{12}	L_{13}	m_2	m_3
770 µH	1.55 µH	1.378 µH	0.9987	1.0607

The value of L_{1k} was used to verify the model, showing a good agreement between the measured value and the theoretical one. The effective turns ratios m_2 and m_3 of the transformer can be measured experimentally from the winding's voltage ratios under open-circuit conditions [6]. This result is also in good agreement with the theoretical values predicted by the model.

III. STUDY OF THE SOC UNBALANCE

Once the transformer model was obtained, it is possible to study the effect of the transformer's parameter dispersion on the *SoC* unbalance of the battery packs. The resonant inverter stage is represented by the current source $\hat{I}_{ac}$ according to (1). The distribution of currents is studied from circuit in Fig. 8 considering the non-ideal transformer.

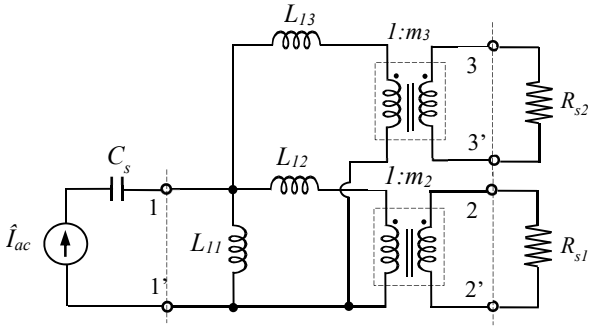

Fig. 8. Equivalent circuit of the output stage to study the current unbalance between both outputs considering a non-ideal transformer.

The equivalent circuit, reduced to primary side, to study the charging current unbalance is shown in Fig. 9.

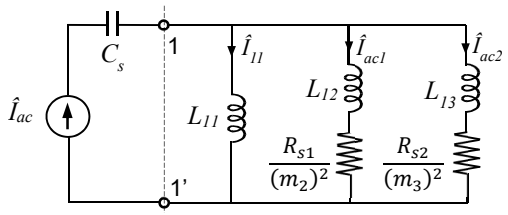

Fig. 9 Equivalent circuit referred to the primary side to study the current sharing between both outputs of the charger considering a non-ideal transformer.

The role of capacitor C_s is DC blocking and is neglected in the study. Unlike the *LLC* converter, the proposed LC_pC_s converter does not require a gapped-core transformer. Thus, the inductance L_{11} is high enough to have little effect on the distribution of currents. Other consideration is that the reflected equivalent impedance of the batteries is ten time higher than the reactance of L_{12} and L_{13} at the switching frequency. According to the rule of the current divider.

$$\frac{\hat{I}_{ac1}}{\hat{I}_{ac2}} = \frac{R_{s2}}{R_{s1}}\left(\frac{m_2}{m_3}\right)^2 \tag{17}$$

Considering the proportionality between the amplitudes of the AC components and the DC values given in (8-10), equation (17) is rewritten as a function of the battery voltages.

$$\frac{m_2}{m_3} = \frac{V_{Bat1}}{V_{Bat2}} \approx \frac{V_{qoc1}(SoC_1)}{V_{qoc2}(SoC_2)} \tag{18}$$

Using data from Table IV, the asymmetries of the transformer's secondary windings lead to a battery voltage unbalance of 5.8%. The battery voltage unbalance has no direct translation into *SoC* unbalance as the curve of the V_{qoc} vs. *SoC* should be considered.

A. Battery model and Simulation

The electrical model [7] of the battery, shown in Fig. 10, is used to observe the variation of the electrical variables during the charging process.

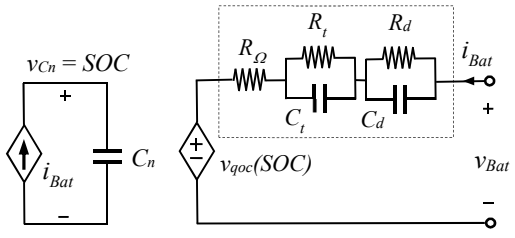

Fig. 10. Battery model based on electric parameters

The electrolyte and electrode resistance are modeled by R_Ω. The model also includes time constants, modeled by networks R_tC_t and R_dC_d. The time constant R_tC_t is associated with chemical reactions and charge transfer phenomenon in the electrodes. The time constant R_dC_d governs the mass transportation in the electrolyte and electrodes. The model is configured with the experimental measurement of the quasi-open-circuit cell voltage, v_{qoc}, as a function of the *SoC* which should be obtained by charging and discharging the battery at a very low current rate, without modifying the electrochemical equilibrium of the battery [7].

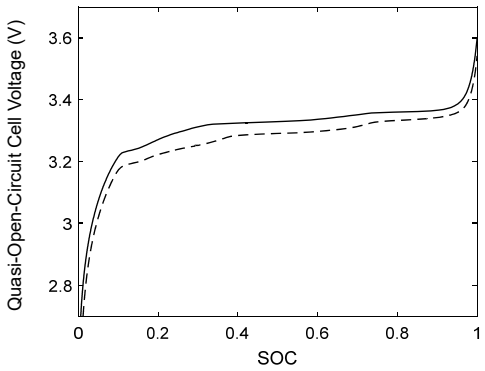

Fig. 11. Quasi-open-circuit voltage of a $LiFePO_4$ cell as a function of the *SOC* obtained at C/50. Solid line: Charging trajectory. Dashed line: Discharging trajectory.

The experimental curve of Fig. 11 results from applying a voltage-controlled voltage source to the model considering that the battery pack is composed by 15 cells. The model is tuned by matching the experimental curve and simulation results. The parameters are shown in Table V.

TABLE V. PARAMETERS OF THE BATTERY MODEL

C_n	R_Ω	R_t	C_t	R_d	C_d
180 kF	9 mΩ	15 mΩ	47.6 F	9 mΩ	333 F

The model was implemented in LTspice. To shorten the simulation time, the battery capacity used in the model C_n was lowered by a scale factor of 500, C_n = 360 F. The effect of the transformer asymmetries on the batteries was studied and the results are shown in Fig. 12.

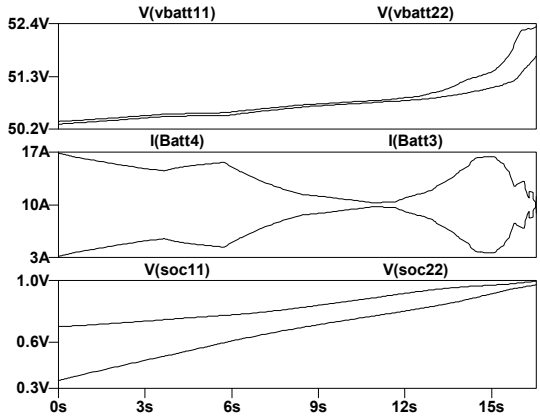

Fig. 12. Simulation results for m_2=0.9987 and m_3=1.067 (mismatch 5.8%) between the secondary windings. From top to bottom: Battery voltages, battery currents and *SoCs*. Axis time x500.

From Fig. 12, an initial $SoC_1 = 0.35$ and $SoC_2 = 0.7$ was considered for each battery pack. At the beginning of the charging process, the heavy *SoC* unbalance commands the current distribution between both battery packs. The module with lower *SoC* naturally receives the higher charging current which never exceeds 20 A. However, at the end of the charging process, the mismatch between the effective transformer ratios m_2 and m_3 defines the final *SoC* unbalance. From Fig. 12, for a windings mismatch of 5.8%, $SoC_1 = 1$ and $SoC_2 = 0.964$.

IV. Experimental Results

The output current capability and efficiency have been experimentally verified with one battery pack. In Fig. 13, the current and voltage at the primary side of the transformer are shown for maximum output power, P_B = 1.07 kW.

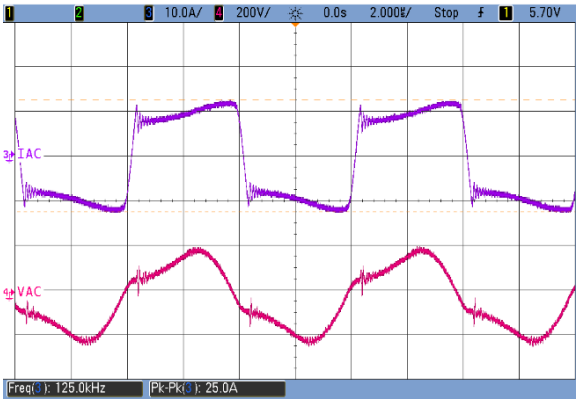

Fig. 13. From top to bottom: Experimental waveforms of the current, i_{ac}, and voltage, v_{ac}, in the primary side of the transformer at maximum output power.

The experimental waveforms to verify the maximum output current capability $I_{Bat(Max)}$ of a single output are shown in Fig. 14. The maximum value of 20 A was obtained. The results are in good agreement with the theoretical value according to the control angle Ψ. It can be observed that the charging current ripple is negligible as it is required for this application.

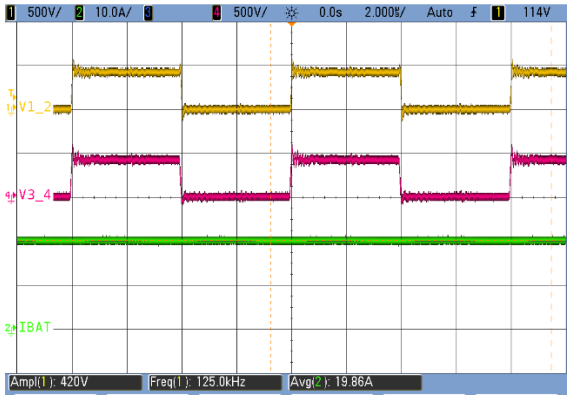

Fig. 14. Experimental waveforms to verify the maximum current capability of a single output achieved at control angle Ψ=0º. From top to bottom: midpoint voltages $v_{1,2}$ and $v_{3,4}$. Charging current.

The worst case of efficiency was measured when only one output provides the maximum charging current (the second output is left open). The efficiency of the prototype, measured under such condition (I_{Bat} = 19.8 A, P_{Bat} = 1.01 kW), was η = 92.3%. The operation at maximum output power with both outputs loaded by a similar load, R_B = 5 Ω, was also evaluated. The results are shown in Fig. 15. The total current is 18.7 A, similar to the obtained in Fig. 14. In this case, the prototype efficiency improved up to η = 94%.

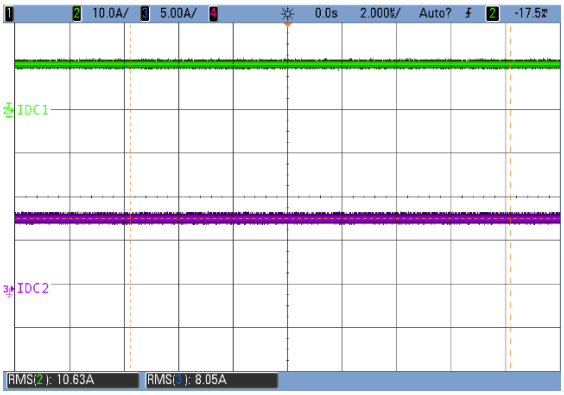

Fig. 15. Output currents provided by each output with a similar load R_B = 5 Ω. Total output power P_B = 1 kW.

V. Conclusions

The multiphase resonant converter capable of charging two $LiFePO_4$ battery packs simultaneously has been presented. The inverter stage is designed as a current source which limits the maximum charging current depending on the battery pack characteristics. The transformer-based equalization is used to achieve *SoC* equalization of the battery modules. The asymmetries of the secondary windings of the transformer must be minimized as they impose a voltage difference between the batteries at the end of the charging process. In this work, the difference of 5.8% between the effective transformer voltage ratios leads to a low 5% of *SoC* unbalance.

Acknowledgment

The authors would like to thank Prof. Manuela Gonzalez and Prof. Juan C. Viera from the Battery Laboratory of University of Oviedo for providing the battery charging profiles and data for tuning the battery model.

References

[1] S. S. Williamson, A. K. Rathore and F. Musavi, "Industrial Electronics for Electric Transportation: Current State-of-the-Art and Future Challenges," in IEEE Trans. on Ind. Elect., vol. 62, no. 5, pp. 3021-3032, May 2015, doi: 10.1109/TIE.2015.2409052.

[2] C. Branas, F. J. Azcondo and R. Casanueva, "A Generalized Study of Multiphase Parallel Resonant Inverters for High-Power Applications," in IEEE Transactions on Circuits and Systems I: Regular Papers, vol. 55, no. 7, pp. 2128-2138, Aug. 2008, doi: 10.1109/TCSI.2008.916704.

[3] S, H. Overview of cell balancing methods for Li-ion battery technology. Energy Storage. 2021; https://doi.org/10.1002/est2.203

[4] Farzan Moghaddam, A.; Van den Bossche, A. A Single Transformer for Active Cell Equalization Method of Lithium-Ion Batteries with Two Times Fewer Secondaries than Cells. Electronics 2019, 8, 951. https://doi.org/10.3390/electronics8090951.

[5] D. Anseán, V. M. García, M. González, J. C. Viera, C. Blanco and J. L. Antuña, "DC internal resistance during charge: Analysis and study on LiFePO4 batteries," 2013 World Electric Vehicle Symposium and Exhibition (EVS27), 2013, pp. 1-11, doi: 10.1109/EVS.2013.6914746.

[6] R. W. Erickson and D. Maksimovic, "A multiple-winding magnetics model having directly measurable parameters," PESC 98 Record. 29th Annual IEEE Power Electronics Specialists Conference (Cat. No.98CH36196), 1998, pp. 1472-1478 vol.2, doi: 10.1109/PESC.1998.703254.

[7] M. Chen and G. A. Rincón-Mora, "Accurate Electrical Battery Model Capable of Predicting Runtime and I-V Performance," IEEE Trans. on Energy Conversion, vol. 21, pp. 504-511, June 2006.